

# Sparse-DFT and WHT Precoding with Iterative Detection for Highly Frequency-Selective Channels

Roberto Bomfin and Marwa Chafii

**Abstract**—Various precoders have been recently studied by the wireless community to combat the channel fading effects. Two prominent precoders are implemented with the discrete Fourier transform (DFT) and Walsh-Hadamard transform (WHT). The WHT precoder is implemented with less complexity since it does not need complex multiplications. Also, spreading can be applied sparsely to decrease the transceiver complexity, leading to sparse DFT (SDFT) and sparse Walsh-Hadamard (SWH). Another relevant topic is the design of iterative receivers that deal with inter-symbol-interference (ISI). In particular, many detectors based on expectation propagation (EP) have been proposed recently for channels with high levels of ISI. An alternative is the maximum a-posteriori (MAP) detector, although it leads to unfeasible high complexity in many cases. In this paper, we provide a relatively low-complexity computation of the MAP detector for the SWH. We also propose two feasible methods based on the Log-MAP and Max-Log-MAP. Additionally, the DFT, SDFT and SWH precoders are compared using an EP-based receiver with one-tap FD equalization. Lastly, SWH-Max-Log-MAP is compared to the (S)DFT with EP-based receiver in terms of performance and complexity. The results show that the proposed SWH-Max-Log-MAP has a better performance and complexity trade-off for QPSK and 16-QAM under highly selective channels, but has unfeasible complexity for higher QAM orders.

**Index Terms**—Single Carrier, Walsh Hadamard, DFT-spread-OFDM, maximum a-posteriori estimation, expectation propagation

## I. INTRODUCTION

SEVERAL waveforms have been investigated in the past years for wireless communications. The most common one employed in modern wireless systems is orthogonal frequency division multiplexing (OFDM) due to its simple frequency-domain (FD) equalization and scalability. However, alternative approaches have been investigated to mitigate the effect of time and/or frequency selective channels [1]–[7]. For instance, a common alternative to OFDM is to perform discrete Fourier transform (DFT) precoding in the frequency domain (FD) symbols. This procedure is called DFT-spread-OFDM and has been used in the uplink of 4G and 5G due to its low peak-to-average power ratio (PAPR) [8]. In this work, we refer to DFT-spread-OFDM as DFT precoding. In addition to the advantageous PAPR aspect of DFT precoding, it effectively allows a higher data rate transmission than OFDM for the same SNR. The authors in [9] have shown that single-carrier (SC), which can be seen as DFT-spread-OFDM with zero padding instead of cyclic prefix (CP), offers a higher data

rate than OFDM. Also, since DFT precoding can be seen as a spreading waveform that spreads the symbols energy in the FD, it maximizes the data rate if the receiver can completely remove inter-symbol interference (ISI) [10]. In this paper, we focus on sparse and full FD precoding for highly frequency-selective channels only, which happens in non line-of-sight (NLoS) propagation environments where the delayed replicas of the transmitted signal have significant power contribution and there is no path with dominant power, e.g., indoor factory scenarios with metal structures and machinery [11]. Nevertheless, as shown in [2], [6], the precoder can be designed to account for time spreading as well, where the energy of symbols are spread along several transmission sub-blocks with each block having a fast Fourier transform (FFT) plus CP size. Therefore, this work could be extended in this direction.

Besides the waveforms based on the DFT precoding such as DFT-spread-OFDM, the Walsh-Hadamard transform (WHT) has been also considered recently as a more attractive precoding alternative from the hardware implementation point of view [4], [5], [12]. This is because WHT requires no complex multiplications to be implemented as opposed to the DFT, while it does achieve the equal gain criterion. Other variants employing WHT-based precoding for doubly dispersive channels using a similar concept to OTFS have been also studied [5], [10]. Another approach to decrease the processing complexity at the receiver side is to employ sparse spreading instead of full spreading. In particular, the authors in [6] have shown that for  $Q > L$ ,  $L$  being the channel length in samples, the spreading can be done sparsely over  $Q$  sub-carriers such that all symbols still experience the same channel gain. The advantage of the sparse spreading is that the receiver now can be implemented with transformations of smaller size, which decreases the complexity regardless of the receiver type. In this paper, we also investigate the impact of sparse spreading for DFT precoding, i.e., sparse DFT (SDFT).

It is known that the spreading waveforms discussed above require iterative equalization in order to take the maximum advantage of the spreading feature [2]–[6], [13]–[15], otherwise, the performance is degraded significantly. This type of receiver was first referred to as turbo equalization in [16], where the same idea of turbo decoding is applied to the equalization process at the symbol level. Although the basic structure of the receiver does not change, there is a vast number of implementation possibilities. For instance, MAP detection [16] computes the exact a-posteriori symbol probability and theoretically represents the best solution in terms of performance, however, this approach leads to unfeasible complexity in general. Alternative approaches employ a linear equalizer (LE) based on the linear minimum mean squared error with

Roberto Bomfin is with the Engineering Division, New York University (NYU) Abu Dhabi, 129188, UAE (email: roberto.bomfin@nyu.edu).

Marwa Chafii is with Engineering Division, New York University (NYU) Abu Dhabi, 129188, UAE and NYU WIRELESS, NYU Tandon School of Engineering, Brooklyn, 11201, NY, USA (email: marwa.chafii@nyu.edu).

parallel interference cancellation (LMMSE-PIC) for the symbol estimation [13], [14], [17]–[20], where the a-priori symbols are used to cancel interference, i.e., coupling among the data symbols. In comparison to the MAP equalizer, the LMMSE-PIC assumes that the data symbols are Gaussian distributed which leads to linear equalization. A more general class of detectors considers an additional expectation propagation (EP)-based step, where the EP-based feedback to the LMMSE equalizer refines the soft symbols estimation [21]–[26]. The EP-based receivers with linear equalization also assume that the symbols are Gaussian distributed, but are superior to the LMMSE-PIC due to an additional refinement process to improve the symbol estimates. In summary, while the MAP based receivers provide significantly better performance than LE for highly frequency-selective channels [13], the EP-based receivers provide a good performance and complexity trade-off between MAP and single LMMSE detection methods [21].

Although the MAP equalizer is typically highly complex, we have derived in our previous work [27] a MAP equalizer with decreased complexity for the SWH waveform of [6]. Differently from the DFT-based transform, the SWH allows independent in-phase and quadrature processing, and it has been shown in [27] that SWH modulation generates amplitudes that belong to a small set. The MAP detector can benefit from this fact to avoid unnecessary multiplications to decrease its complexity. However, our work in [27] does not discuss the computation of the exponential terms in the symbols marginalization, or log-likelihood ratios (LLRs) computation, which can be a bottleneck in terms of complexity since the exponential function requires multiplications to be implemented. In this paper, two feasible methods based on the Log-MAP and Max-Log-MAP [28] are investigated that avoids computing the exponential function explicitly. The Log-MAP method directly computes the extrinsic LLRs by evaluating the logarithm of exponential summation (LogSumExp) recursively. This method uses a pre-stored table which avoids the explicit computation of the exponential and logarithm functions. The Max-Log-MAP solution avoids the look-up table operation and reduces the complexity by approximating the LogSumExp by the maximum argument of the exponential functions. Although the overall complexity is considerably reduced due to a small number of multiplications, the number of additions to compute the extrinsic LLRs can still be prohibitively high depending on the system parameters. This bottleneck is identified in this paper and a future research direction to mitigate this issue is given.

There have been many works on EP-based receivers. In particular, authors in [21] have proposed a self-iterated frequency domain (FD) linear equalizer-interference cancellation with EP-based feedback (SILE-EPIC) applied to the DFT precoded system, where the data symbols are assumed to belong to a multivariate white Gaussian distribution. This assumption allows the one-tap equalization step in FD, which considerably decreases the receiver's complexity. A similar idea has been reported in [14] for the LMMSE-PIC, where this simplification leads to no performance loss. Most importantly, the SILE-EPIC of [21] provides a better performance and complexity trade-off than other EP-based receivers. In

particular, the receivers in [25], [26] are sub-optimal due to a single self-iteration (SI) and absence of damping. The receiver of [24] slightly outperforms the SILE-EPIC, but with much higher computational complexity. Moreover, the SILE-EPIC has shown superior performance than the generalized approximate message passing (GAMP) [29] and vector AMP (VAMP) [30] with extrinsic output. Thus, in this work, we use the SILE-EPIC of [21] as the FD EP-based benchmark receiver. We highlight that other precoders besides DFT have not been evaluated in the original SILE-EPIC paper. Thus, in this work, we modify the SILE-EPIC to work with the SDFT and SWH precoders, where detailed performance and complexity comparisons among these precoders are provided. In particular, we show that the SDFT system has a smaller mean squared error of the estimated symbols than the DFT system, which leads to slightly better performance.

In this paper, we provide two feasible methods based on the Log-MAP and Max-Log-MAP for the SWH precoder. Additionally, the DFT, SDFT, and SWH precoders are compared using SILE-EPIC receivers with one-tap FD equalization. Lastly, SWH-Max-Log-MAP is compared to the (S)DFT with EP-based receiver in terms of performance and complexity.

The contributions of this paper are summarized as follows:

- Extend our work in [27] regarding the MAP detector for the SWH, by developing and analyzing two feasible methods that avoid the computation of exponential terms in the LLR computation, namely, the Log-MAP and Max-Log-MAP. The results show that the Max-Log-MAP presents a small performance loss and the Log-MAP performs equally to the exact one of [27].
- Complement the work of [21] by extending the SILE-EPIC receiver to operate with SDFT and WHT precoders. The results show that the sparse precoders decrease the receiver's complexity due to the transformation of smaller size, which is more significant for quadrature phase-shift keying (QPSK). In terms of performance, it is shown that the SDFT provides slightly better performance than DFT.
- Provide a complexity analysis of Log-MAP and Max-Log-MAP equalizers for SWH, and SILE-EPIC in terms of multiplications and additions per QAM symbol, such that the different methods can be compared fairly.
- Provide a detailed performance vs. complexity trade-off comparison between DFT and WHT-based precoders employing the SILE-EPIC or MAP-based receivers. The results show that SWH-Max-Log-MAP has a better performance and complexity trade-off for QPSK and 16-QAM, while for higher QAM orders it has unfeasible complexity.

The remainder of this paper is organized as follows. In Section II, we provide a general description of the system model in FD. In Section III, the system model for the sparse precoders is given in detail. In Section IV, the Log-MAP and Max-Log-MAP methods are provided. In Section V, the SILE-EPIC receiver of [21] is described and the modifications for SDFT and SWH are provided. In Section VI, a detailed complexity analysis in terms of real additions and multiplica-

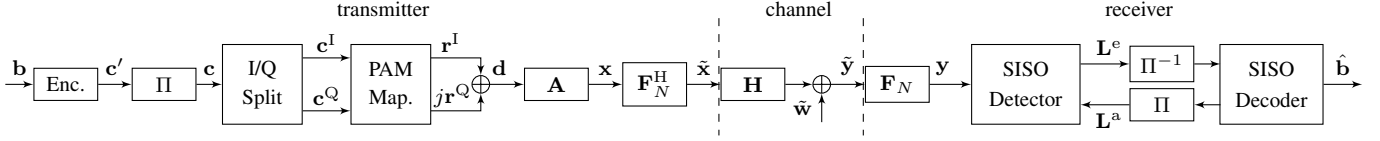


Fig. 1. Block diagram of the system model including transmitter, channel and receiver.

tions per quadrature amplitude modulation (QAM) symbol is given for the SWH-MAP and SILE-EPIC receivers. In Section VII, a numerical evaluation is provided for performance and complexity analysis. Finally, Section VIII concludes the paper and provide ideas for future research.

*Notations:* column vectors are described as lower case bold symbols as  $\mathbf{x}$  whose  $n$ th element is  $x_n$ . Matrices are described as upper case bold symbols as  $\mathbf{X}$ , whose element in the  $n$ th row and  $m$ th column is given by  $X_{n,m}$ . The transpose and conjugate transpose are defined respectively as  $(\cdot)^T$  and  $(\cdot)^H$ . The QAM and pulse amplitude modulation (PAM) sets are defined respectively as  $\mathcal{D}$  and  $\mathcal{R}$ . The set of complex number is defined as  $\mathbb{C}$ . The  $N \times N$  matrices  $\mathbf{I}_N$ ,  $\mathbf{F}_N$  and  $\mathbf{W}_N$  represent the identity, normalized Fourier and Walsh-Hadamard matrices, respectively, such that  $\mathbf{F}_N^H \mathbf{F}_N = \mathbf{W}_N^H \mathbf{W}_N = \mathbf{I}_N$ . Other functions and symbols are defined as they occasionally appear.

## II. SYSTEM MODEL

### A. Transmitter

The transmitter employs a bit-interleaved coded modulation (BICM) transmission [31]. As depicted in the transmitter part of Fig. 1, a vector of information bits  $\mathbf{b} \in \{0, 1\}^{N_b}$  is encoded creating the coded bit stream  $\mathbf{c}' = \text{enc}(\mathbf{b}) \in \{0, 1\}^{N_c}$ , where  $\text{enc}(\cdot)$  represents the encoder. The quantities  $R = N_b/N_c$ ,  $N_b$  and  $N_c$  represent the coding rate, number of uncoded and coded bits, respectively. Subsequently, the coded bits  $\mathbf{c}$  are interleaved as  $\mathbf{c} = \Pi(\mathbf{c}')$ , where  $\Pi(\cdot)$  represents the interleaver. As shown in Fig. 1, the vector of coded bits is split into two sub-vectors  $\mathbf{c}^I = [c_0 \ c_1 \ \dots \ c_{\frac{N_c}{2}-1}]^T$ ,  $\mathbf{c}^Q = [c_{\frac{N_c}{2}} \ c_{\frac{N_c}{2}+1} \ \dots \ c_{N_c-1}]^T \in \{0, 1\}^{\frac{N_c}{2}}$ , which are mapped respectively onto the in-phase and quadrature PAM symbols  $\mathbf{r}^I, \mathbf{r}^Q \in \mathcal{R}^N$ , where  $\mathcal{R}$  denotes the set of a PAM constellation with cardinality  $|\mathcal{R}| = \sqrt{J}$ . The QAM symbols can be defined as  $\mathbf{d} = \mathbf{r}^I + jr^Q \in \mathcal{D}^N$ , where  $\mathcal{D}$  is the QAM set with cardinality  $|\mathcal{D}| = J$ .

In general, the QAM symbols are modulated with the FD precoding matrix  $\mathbf{A} \in \mathbb{C}^{N \times N}$  as

$$\mathbf{x} = \mathbf{A}\mathbf{d}, \quad (1)$$

where the modulated signal in the time domain is obtained by performing the inverse FFT as  $\tilde{\mathbf{x}} = \mathbf{F}_N^H \mathbf{x}$ . In this work, we consider three options for the matrix  $\mathbf{A}$ .

1) *sparse Walsh-Hadamard (SWH):*  $\mathbf{A}_{\text{SW}} = \mathbf{W}_Q \otimes \mathbf{I}_P$ ,  $QP = N$ ,  $\mathbf{W}_Q$  is the normalized Walsh-Hadamard matrix of

size  $Q$ ,

$$\mathbf{W}_Q = \mathbf{W}_2 \otimes \mathbf{W}_{Q/2}, \quad \mathbf{W}_2 = \frac{1}{\sqrt{2}} \begin{bmatrix} 1 & 1 \\ 1 & -1 \end{bmatrix} \quad (2)$$

and  $\otimes$  is the Kronecker product. As it has been shown in [6], the precoder  $\mathbf{A}$  ensures equal channel gain for the elements of  $\mathbf{d}$  for  $Q \geq L$ , where  $L$  is the channel length. A detailed description of the sparse spreading precoder is given in Section III.

2) *DFT:*  $\mathbf{A}_F = \mathbf{F}_N$  is defined as the DFT matrix of size  $N$ . Notice that this is the same as the DFT-spread modulation, sometimes also referred to as single-carrier.

3) *SDFT:*  $\mathbf{A}_{\text{SF}} = \mathbf{F}_Q \otimes \mathbf{I}_P$ . This modulation follows the same principle as the SWH of [6], but with the WHT being replaced by the DFT.

### B. Received Signal

Assuming perfect time and frequency synchronization, and proper CP insertion/removal, the discrete-time received signal in the time domain  $\tilde{\mathbf{y}} \in \mathbb{C}^N$  is given by

$$\tilde{\mathbf{y}} = \mathbf{H}\tilde{\mathbf{x}} + \tilde{\mathbf{w}}, \quad (3)$$

where  $\mathbf{H} \in \mathbb{C}^{N \times N}$  is a circulant matrix whose first column is defined by the channel impulse response  $\mathbf{h}$  and  $\tilde{\mathbf{w}} \sim \mathcal{CN}(0, \mathbf{I}_N \sigma^2)$  is the additive white Gaussian noise (AWGN) with power  $\sigma^2$ . The above signal is depicted in the channel part in Fig. 1. In the frequency domain, the received signal is given in double column version

$$\mathbf{y} = \mathbf{F}_N \tilde{\mathbf{y}} \\ = \mathbf{\Lambda} \mathbf{A} \mathbf{d} + \mathbf{w}, \quad (4)$$

where  $\mathbf{\Lambda} = \mathbf{F}_N \mathbf{H} \mathbf{F}_N^H \in \mathbb{C}^{N \times N}$  is the diagonal channel matrix whose elements correspond to the channel response in the frequency domain. The component  $\mathbf{w} \sim \mathcal{CN}(0, \mathbf{I}_N \sigma^2)$  is the AWGN with power  $\sigma^2$  in frequency domain. The second line of (4) is obtained by substituting  $\tilde{\mathbf{x}} = \mathbf{F}_N^H \mathbf{x} = \mathbf{F}_N^H \mathbf{A} \mathbf{d}$  from (1).

### C. Iterative Receiver

A generic structure of the iterative receiver is depicted in the right most part of Fig. 1, where perfect channel knowledge and noise variance are known<sup>2</sup>. There are basically two main structures that compose this receiver, namely, the single-input single-output (SISO) detector and the SISO decoder.

<sup>2</sup>We note that in case of imperfect channel knowledge, the system in (4) could be modeled with an additional noise term w.r.t. to the channel estimation error as in [2], which in turn changes the SNR operating point of the system, and does not fundamentally change the design of the equalizer.

<sup>1</sup>In this paper we neglect the parameter  $Q'$  of [6] because we consider a time invariant channel model.

In this work, we focus on the SISO detector which has the purpose of estimating extrinsic bit LLRs,  $\mathbf{L}^e$ , given the received signal, channel response, noise power and a-priori bit LLRs,  $\mathbf{L}^a$ . The terms extrinsic and a-priori LLRs are defined from the detector's perspective. In this work, we consider iterative receivers with two classes of detectors. The first class is based on the MAP detector for the SWH which is described in Section IV. The second class of detectors is the self-iterated linear equalizer with expectation propagation (SILE-EPIC) of [21], which is an EP-based receiver with one-tap FD equalization. This receiver performs self-iterations between the LMMSE equalizer and the mapper/demapper nodes based on the expectation propagation (EP) method, which drastically improves the performance under highly selective channels.

The other component is the SISO decoder, which updates the coded bit LLRs to the detector node based on its input bit LLRs. In order to respect the turbo principle of not using the same information twice,  $\mathbf{L}^a$  is computed by subtracting  $\mathbf{L}^e$  from the decoder's a-posteriori probability (APP) estimation. In this work, we employ the recursive systematic convolutional (RSC) encoder with Bahl, Cocke, Jelinek, and Raviv (BCJR) SISO decoding.

### III. SPARSE PRECODERS SYSTEM MODEL

In this section, we present the system model for SWH and SDFM precoders, which is necessary to describe their respective receivers. In the following, we consider the SWH precoder  $\mathbf{A}_{\text{SW}} = \mathbf{W}_Q \otimes \mathbf{I}_P$ , but the model is directly applicable to the DFT precoder by replacing  $\mathbf{W}_Q$  by  $\mathbf{F}_Q$  as mentioned in Section II-A.

#### A. Modulation

One way to describe the sparsity of  $\mathbf{A}_{\text{SW}}$  is to group  $P$  different sub-vectors with  $Q$  data symbols each. The data symbols of each sub-vector are spread over the same set of sub-carriers. These sub-vectors are defined as  $\mathbf{d}_p = [d_p d_{p+P} d_{p+2P} \cdots d_{p+P(Q-1)}]^T \in \mathcal{D}^Q$  for  $p = 0, 1, \dots, P-1$ . It is possible to show that the symbols of  $\mathbf{d}_p$  are spread among the carriers with the same index as the symbols as

$$I_p = \{p + qP | q \in \{0, 1, \dots, Q-1\}\}. \quad (5)$$

This is illustrated in Fig. 2 by depicting the non-normalized matrix  $\tilde{\mathbf{A}}_{\text{SW}}$  with  $N = 8$  sub-carriers,  $Q = 4$  symbols per sub-group and  $P = 2$  groups. Notice that the columns and rows of  $\tilde{\mathbf{A}}_{\text{SW}}$  are associated with the symbols and sub-carriers, respectively. The symbol sub-vectors are defined as  $\mathbf{d}_0 = [d_0 d_2 d_4 d_6]^T$  and  $\mathbf{d}_1 = [d_1 d_3 d_5 d_7]^T$  for  $p = 0$  and  $p = 1$ , respectively. Then, one can verify that the modulation  $\mathbf{A}_{\text{SW}}\mathbf{d}$  in (1) spreads the symbols with indexes  $I_0 \in \{0, 2, 4, 6\}$  among the carriers with the same indexes  $I_0$ .

Additionally, we can define the sparse modulation as in Fig. 3 which is compactly written as

$$\mathbf{x} = \text{vec}_N \left( (\mathbf{W}_Q (\text{unvec}_{Q \times P}(\mathbf{d}^T)))^T \right). \quad (6)$$

The modulated data is computed in three steps, namely, i) stack the sub-vectors  $[\mathbf{d}_0 \mathbf{d}_1 \cdots]$  with the operation  $\text{unvec}_{Q \times P}(\mathbf{d}^T)$ ,

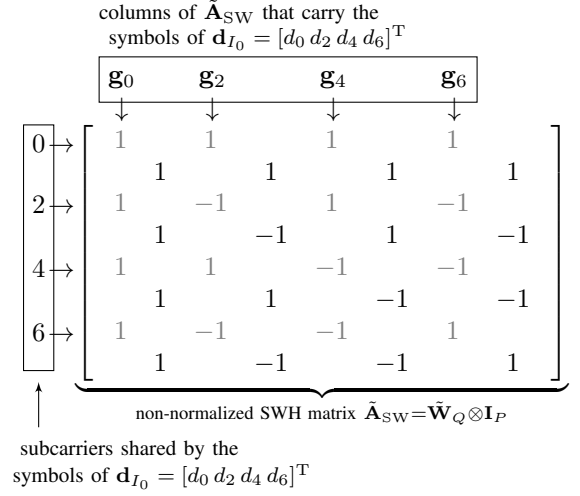


Fig. 2. Example of  $\mathbf{A}_{\text{SW}}$ :  $N = 8$ ,  $Q = 4$  and  $P = 2$ , where the elements of  $\mathbf{d}_0 = [d_0 d_2 d_4 d_6]^T$  share the same sub-carriers with indexes  $I_0 \in \{0, 2, 4, 6\}$ . The zeros of the SWH matrix  $\tilde{\mathbf{A}} = \tilde{\mathbf{W}}_Q \otimes \mathbf{I}_P$  are replaced with spaces for clearness and  $\mathbf{g}_n$  is the  $n$ th columns of  $\tilde{\mathbf{A}}_{\text{SW}}$ .

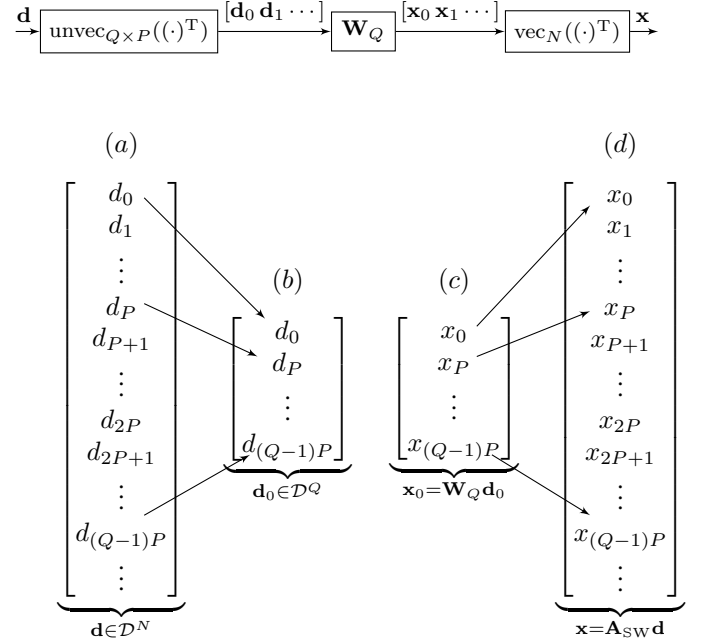


Fig. 3. (Top) Sparse modulation diagram  $\mathbf{x} = \mathbf{A}_{\text{SW}}\mathbf{d}$ . (Bottom) Representation of unvec and vec operations for  $p = 0$ , (a) data vector, (b) data sub-vector after unvec operation, (c) modulation per sub-vector, (d) sparse modulated data after vec operation.

ii) modulate the sub-vectors as  $[\mathbf{x}_0 \mathbf{x}_1 \cdots] = \mathbf{W}_Q[\mathbf{d}_0 \mathbf{d}_1 \cdots]$ , and iii) create an  $N \times 1$  vector representing the modulated signal as  $\mathbf{x} = \text{vec}_N([\mathbf{x}_0 \mathbf{x}_1 \cdots]^T)$ .

#### B. Received Signal

Since the received signal in the equation (4) is already in FD, we can build its sub-vectors in analogy to  $\mathbf{d}_p$  as  $\mathbf{y}_p = [y_p y_{p+P} \cdots y_{p+P(Q-1)}]^T \in \mathbb{C}^{Q \times 1}$  for  $p = 0, 1, \dots, P-1$ , which is modeled as

$$\mathbf{y}_p = \mathbf{\Lambda}_p \mathbf{W}_Q \mathbf{d}_p + \mathbf{w}_p. \quad (7)$$

The channel matrix and noise can be split accordingly as  $\mathbf{\Lambda}_p = \text{diag}([\Lambda_{p,p} \Lambda_{p+P,p+P} \cdots \Lambda_{p+P(Q-1),p+P(Q-1)}]) \in \mathbb{C}^{Q \times Q}$  has the channel components in its diagonal whose indexes belong to  $I_p$ , and  $\mathbf{w}_p = [w_p w_{p+P} \cdots w_{p+P(Q-1)}]^T \sim \mathcal{N}(0, \mathbf{I}_Q \sigma^2)$ , respectively.

#### IV. MAP DETECTORS FOR THE SWH

##### A. Channel Phase Correction

As shown in [27], in order to build an equalizer with independent in-phase and quadrature processing, the phase of the received signal  $\mathbf{y}_p$  in the equation (7) is corrected such that its real and imaginary components are exclusively associated with the in-phase and quadrature dimensions of the QAM constellation, respectively. This can be done by correcting the channel phase rotation as

$$\mathbf{y}'_p = \frac{\mathbf{\Lambda}_p^H}{|\mathbf{\Lambda}_p|} \mathbf{y}_p = |\mathbf{\Lambda}_p| \mathbf{W}_Q (\mathbf{r}_p^I + j\mathbf{r}_p^Q) + \mathbf{v}'_p, \quad (8)$$

where  $\mathbf{v}'_p \sim \mathcal{CN}(0, \mathbf{I}_Q \sigma^2)$  is the noise with phase rotation and has its statistics unchanged in relation to  $\mathbf{v}_p$  in (7). Also,  $|\mathbf{\Lambda}_p|$  returns the element-wise absolute values of  $\mathbf{\Lambda}_p$ . Since the modulation matrix  $\mathbf{W}_Q$  does not introduce any phase rotation in the data symbols, it is straightforward to observe that  $\mathbf{y}'_p = \text{Re}(\mathbf{y}'_p)$  and  $\mathbf{y}'_p = \text{Im}(\mathbf{y}'_p)$  exclusively carry information of the in-phase and quadrature components associated to the PAM constellation, respectively, as shown below

$$\mathbf{y}'_p^I = |\mathbf{\Lambda}_p| \mathbf{W}_Q \mathbf{r}_p^I + \mathbf{w}'_p^I, \quad \mathbf{y}'_p^Q = |\mathbf{\Lambda}_p| \mathbf{W}_Q \mathbf{r}_p^Q + \mathbf{w}'_p^Q. \quad (9)$$

Thus, the MAP-based receivers for the SWH precoder operate directly on the received signal defined in (9).

##### B. Exact MAP Detector [27]

In the following, the detector estimation is described for the symbols and bits associated with the in-phase PAM symbols without loss of generality, since the same analysis applies to the quadrature component. As shown in Appendix A, we can write the conditional probability below

$$\begin{aligned} p(\mathbf{y}'_p^I | \mathbf{z}) &\propto \exp\left(-\frac{1}{\sigma^2} \|\mathbf{y}'_p^I - |\mathbf{\Lambda}_p| \mathbf{W}_Q \mathbf{z}\|^2\right) \\ &= \exp\left(\sum_{\substack{q'=0, \\ i=\mathcal{S}(\mathbf{z}, q)}}^{Q-1} C_p^I(q', i)\right), \end{aligned} \quad (10)$$

“for a given PAM vector realization  $\mathbf{z} \in \mathcal{R}^Q$ . The quantity  $C_p^I(q, i)$  is given by

$$C_p^I(q, i) = -(\mathbf{y}'_p^I[q] - |\mathbf{\Lambda}_p[q, q]| s_i)^2 / \sigma^2, \quad (11)$$

for  $q \in \{0, 1, \dots, Q-1\}$  and  $i \in \{0, 1, \dots, Q(\sqrt{J}-1)\}$ , where

$$s_i = (-Q(M-1) + 2i) / \sqrt{Q} \quad (12)$$

is based on the set  $\mathcal{U}$  defined in Appendix A. The advantage defining  $C_p^I(q, i)$  in (11) is that it allows the computation of  $p(\mathbf{y}'_p^I | \mathbf{z})$  in a simplified manner as the second line of (10). We

note that  $C_p^I(q, i)$  should be computed for each channel realization, however, since  $i \in \{0, 1, \dots, Q(\sqrt{J}-1)\}$ , there are  $Q(\sqrt{J}-1) + 1$  values to be computed per PAM symbol, which does not represent a bottleneck in terms of complexity. More details are given in Section VI. In (10),  $\mathcal{S}(\mathbf{z}, q) = \{i | u_q = s_i\}$  returns the index  $i$  which attains the condition  $u_q = s_i$  and can be interpreted as a database which stores the respective values for all  $\mathbf{z} \in \mathcal{R}^Q$  and  $q \in \{0, 1, \dots, Q-1\}$ , where  $\mathbf{u} = \mathbf{W}_Q \mathbf{z}$ .

In summary, the values  $C_p^I(q, i)$  are computed beforehand and then reused for each new  $\mathbf{z}$ , which allows the receiver to avoid most of the complex multiplications in relation to the general MAP formulation. On the contrary, if the quantity  $\|\mathbf{y}'_p^I - |\mathbf{\Lambda}_p| \mathbf{W}_Q \mathbf{z}\|^2$  is computed for each  $\mathbf{z}$  in its general form in (10), the calculations of (11) are unnecessarily computed multiple times because the possible values of the elements of the modulated symbols  $\mathbf{W}_Q \mathbf{z}$  are taken from a small set.

In general, the MAP estimation of the in-phase or quadrature PAM data symbols is computed as

$$\begin{aligned} p_{p,q}^I(\mathbf{r}) &= p(\mathbf{r}_{p,q}^I = \mathbf{r} | \mathbf{y}'_p^I) \\ &\propto \sum_{\substack{\mathbf{z} \in \mathcal{R}^Q, \\ \mathbf{z}_q = \mathbf{r}}} p(\mathbf{y}'_p^I | \mathbf{z}) p_{p,q}^{\text{a},I}(\mathbf{r}^I = \mathbf{z}), \end{aligned} \quad (13)$$

for  $q \in \{0, 1, \dots, Q-1\}$ ,  $p \in \{0, 1, \dots, P-1\}$  where  $p(\mathbf{y}'_p^I | \mathbf{z})$  is given in (10) and the a-priori symbol probability under the assumption of independent bits is given by

$$p_{p,q}^{\text{a},I}(\mathbf{r}^I = \mathbf{z}) = \prod_{q=0}^{Q-1} \prod_{b=0}^{\frac{1}{2} \log_2 J - 1} \exp\left(\phi_b^{-1}(z_q) L_{p,q,b}^{\text{a},I}\right), \quad (14)$$

where  $\phi_b^{-1}(z)$  is a demapper which returns 1 or 0 if the  $b$ th bit of the PAM symbol  $z \in \mathcal{R}$  is 0 or 1, respectively. For completeness, the indexes  $p$ ,  $q$  and  $b$  of  $L_{p,q,b}^{\text{a},I}$  correspond to the  $p$ th sub-vector,  $q$ th symbol and  $b$ th bit. The posterior symbol probability in (13) can be written as (15) by combining (10) with (14). Lastly, the extrinsic LLRs are computed by combining (15) with

$$L_{p,q,b}^{\text{e},I} = \ln \frac{\sum_{\mathbf{r} \in \mathcal{R}_b^{(0)}} p_{p,q}^I(\mathbf{r})}{\sum_{\mathbf{r} \in \mathcal{R}_b^{(1)}} p_{p,q}^I(\mathbf{r})} - L_{p,q,b}^{\text{a},I}, \quad (16)$$

where  $\mathcal{R}_b^{(0)} = \{z \in \mathcal{R} | \phi_b(z)^{-1} = 0\}$  is the set containing all PAM symbols whose  $b$ th is 0, and  $\mathcal{R}_b^{(1)}$  is the equivalent set for the bit 1.

The issue of computing the LogSumExp in (16) in combination with (15) is not discussed in [27]. Thus, in the following we provide two feasible approaches to tackle this problem, namely, the Log-MAP and Max-Log-MAP [28] methods.

##### C. Log-MAP Detector

For the MAP-Log detector, we are not interested in the intermediate symbol marginalization in (15), but in computing

$$p_{p,q}^I(\mathbf{r}) \propto \sum_{\substack{\mathbf{z} \in \mathcal{R}^Q \\ z_q = r}} \exp \left( \sum_{\substack{q'=0 \\ i=S(\mathbf{z},q')}}^{Q-1} \left( C_p^I(q',i) - \sum_{b=0}^{\frac{1}{2} \log_2(J)-1} \phi_b^{-1}(z_{q'}) L_{p,q',b}^{a,I} \right) \right) \quad (15)$$

the extrinsic LLRs directly. In order to allow this computation, the following variable is defined

$$t_p^I(\mathbf{z}) = \sum_{\substack{q'=0 \\ i=S(\mathbf{z},q')}}^{Q-1} \left( C_p^I(q',i) - \sum_{b=0}^{\frac{1}{2} \log_2(J)-1} \phi_b^{-1}(z_{q'}) L_{p,q',b}^{a,I} \right), \quad (17)$$

which is essentially the exponential argument in the equation (15) for a given  $\mathbf{z} \in \mathcal{R}^Q$ . Then, the extrinsic LLRs of (16) are written as a function of  $t_p^I(\mathbf{z})$  as follows

$$L_{p,q,b}^{e,I} = \ln \left( \sum_{\mathbf{z} \in \mathcal{R}_{q,b,0}^Q} \exp(t_p^I(\mathbf{z})) \right) - \ln \left( \sum_{\mathbf{z} \in \mathcal{R}_{q,b,1}^Q} \exp(t_p^I(\mathbf{z})) \right) - L_{p,q,b}^{a,I}, \quad (18)$$

where the set  $\mathcal{R}_{q,b,0}^Q = \{\mathbf{z} \in \mathcal{R}^Q | \phi_b(z_q)^{-1} = 0\}$  contains all realizations of  $\mathbf{z}$  in which the  $b$ th bit of  $z_q$  equals 0, and  $\mathcal{R}_{q,b,1}^Q$  has the same definition for the bit 1.

When computed in closed form, the Log-MAP method provides an exact computation of the MAP detector based on the LogSumExp relation

$$\ln(e^{\delta_0} + e^{\delta_1}) = \max(\delta_0, \delta_1) + \ln(1 + e^{-|\delta_0 - \delta_1|^2}). \quad (19)$$

If we write  $e^\delta = e^{\delta_0} + e^{\delta_1}$ , we can compute  $\ln(e^{\delta_0} + e^{\delta_1} + e^{\delta_2}) = \ln(e^\delta + e^{\delta_2}) = \max(\delta, \delta_2) + \ln(1 + e^{-|\delta - \delta_2|^2})$  using (19). Since this process always accepts a new term to the sum of exponential [28], the desired expression  $\ln(e^{\delta_0} + e^{\delta_1} + \dots + e^{\delta_{N-1}})$  can be computed exactly in (18).

Notice that the term  $f_c(|\delta_0 - \delta_1|) = \ln(1 + e^{-|\delta_0 - \delta_1|^2})$  in (19) is still not friendly for practical implementation. Thus, one solution is to store the values of  $f_c(\cdot)$  in a table, such that  $\ln(\cdot)$  and  $\exp(\cdot)$  are not invoked as discussed in [28]. The quality of this approximation depends on how many values of  $f_c(\cdot)$  are stored. In the numerical evaluation of Section VII, we use 256 values for  $f_c(x)$  uniformly spaced in the range  $0 \leq x \leq 10$ , which is sufficient to provide a performance as good as the exact one.

#### D. Max-Log-MAP Detector

The Max-Log-MAP algorithm is a sub-optimal solution that takes the maximum argument of the exponential terms as  $\ln(e^{\delta_0} + e^{\delta_1} + \dots + e^{\delta_{N-1}}) \approx \max_i \delta_i$ . The Max-Log-MAP detector simply computes

$$L_{p,q,b}^{e,I} = \max_{\mathbf{z} \in \mathcal{R}_{q,b,0}^Q} (t_p^I(\mathbf{z})) - \max_{\mathbf{z} \in \mathcal{R}_{q,b,1}^Q} (t_p^I(\mathbf{z})) - L_{p,q,b}^{a,I}. \quad (20)$$

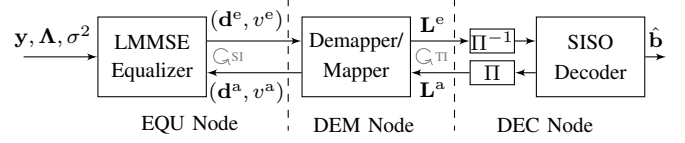


Fig. 4. Block diagram of SILE-EPIC receiver of [21].

The differences with the Log-MAP detector are that the Max-Log-MAP method does not require the additions involved in the argument of  $f_c(|\delta_0 - \delta_1|)$ , and it does not require the look-up table operations.

## V. SILE-EPIC DETECTOR

In this section, the SILE-EPIC receiver presented in [21] is described. Assuming independent and identically distributed (i.i.d.) information bits, and focusing on the joint estimation of the data symbols  $d_n$  and coded bits  $c_{n,b}$ , we can write the posterior probability factorization

$$p(\mathbf{c}, \mathbf{d} | \mathbf{y}) = p(\mathbf{y} | \mathbf{d}) \prod_{n=0}^{N-1} p(d_n | \mathbf{c}_n) \prod_{b=0}^{K-1} p(c_{n,b}), \quad (21)$$

from which the channel, mapping, and coding constraints are observed, which are respectively related to the terms  $p(\mathbf{y} | \mathbf{d})$ ,  $p(d_n | \mathbf{c}_n)$  and  $\prod_{b=0}^{K-1} p(c_{n,b})$ . In the context of a factor graph model, these constraints respectively define the factor nodes (FNs) *EQU Node*, *DEM Node*, and *DEC Node*. As such, this iterative receiver works as a message-passing algorithm that operates on the variables  $d_n$  and  $c_{n,b}$  with the constraints determined by the FN's.

In the following, we directly describe the messages derived in [21] between the factor and variable nodes. A diagram of the SILE-EPIC detector is depicted in Fig. 4.

#### A. Messages for DFT Precoder

1) *Messages from DEC to DEM*: As discussed in the Subsection II-C, the DEC node is a SISO decoder that feeds back a-priori LLRs  $L^a$  to the DEM. Considering the mapping constraint, the prior probability mass function (PMF) of  $d_n$  is computed as

$$P_n(d) \propto \prod_{b=0}^{\log_2 J - 1} \exp(-\phi_b^{-1}(d) L_{n,b}^{a,I}), \quad \forall d \in \mathcal{D}. \quad (22)$$

For completeness, the indexes  $n$  and  $b$  of  $L_{n,b}^{a,I}$  correspond to the  $n$ th QAM symbol and  $b$ th bit.

2) *Messages from DEM to EQU*: This subsection describes how the variables  $(\mathbf{d}^a, v^a)$  in Fig. 4 are updated, given that the DEM has the PMF in (22) and the variables  $(\mathbf{x}^e, v^e)$  as inputs. Firstly, the DEM node computes the posterior symbol PMF as

$$D_n(\mathbf{d}) \propto \exp(-|\mathbf{d} - \mathbf{d}_n^e|^2/v^e)P_n(\mathbf{d}), \quad \forall \mathbf{d} \in \mathcal{D}, \quad (23)$$

from which the moments are computed as

$$\mu_n^a = \sum_{\mathbf{d} \in \mathcal{D}} \mathbf{d} D_n(\mathbf{d}), \quad (24)$$

and

$$\gamma_n^a = \sum_{\mathbf{d} \in \mathcal{D}} |\mathbf{d}|^2 D_n(\mathbf{d}) - |\mu_n^a|^2. \quad (25)$$

Since the receiver assumes that the variable nodes related to  $\mathbf{d}$  are multivariate white Gaussian random variables, the second moment of all elements of  $\mathbf{d}$  are approximated to the mean

$$\bar{\gamma}^a = \frac{1}{N} \sum_{n=0}^{N-1} \gamma_n^a. \quad (26)$$

The variable pair  $(d_n^*, v^*)$  is derived by dividing the PDF  $\mathcal{CN}(\mu_n^a, \gamma^a)$  by  $\mathcal{CN}(d_n^e, \gamma^e)$ , which results in

$$d_n^* = \frac{\mu_n^a v^e - d_n^e \bar{\gamma}^a}{v^e - \bar{\gamma}^a}, \quad \text{and} \quad v^* = \frac{v^e \bar{\gamma}^a}{v^e - \bar{\gamma}^a}. \quad (27)$$

The scheme above can lead to negative variance when  $\bar{\gamma}^a > v^e$ . In this case, we use the values  $(d_n^a, v^a)$  as [21].

As highlighted in [21], using  $(d_n^*, v^*)$  directly as feedback leads to detrimental local extrema. To circumvent this problem, the linear smoothing procedure below is used

$$\begin{aligned} d_n^{\text{a(next)}} &= (1 - \beta)d_n^* + \beta d_n^{\text{a(prev)}} \\ v^{\text{a(next)}} &= (1 - \beta)v^* + \beta v^{\text{a(prev)}}, \end{aligned} \quad (28)$$

for  $0 \leq \beta \leq 1$ . We set  $\mathbf{d}^{\text{a(prev)}} = \mathbf{0}_N$  and  $v^{\text{a(prev)}} = 1$  at the beginning of each new self-iteration between DEM and EQU.

3) *Messages from EQU to DEM*: This subsection describes how the EQU node updated the variables  $(\mathbf{d}^e, v^e)$ , given that it has  $(\mathbf{d}^a, v^a)$  as input from the DEM node. The equalization process of the EP based receiver turns out to be equivalent to the component wise conditionally unbiased (CWCU) LMMSE [14], [32], which is an unbiased estimator, where the symbol mean and error variance are computed as

$$\mathbf{d}^e = \mathbf{d}^a + \frac{1}{\lambda} \mathbf{F}_N^H \mathbf{\Lambda}^H (\mathbf{\Lambda} \mathbf{\Lambda}^H v^a + \sigma^2 \mathbf{I}_N)^{-1} (\mathbf{y} - \mathbf{\Lambda} \mathbf{F}_N \mathbf{d}^a) \quad (29)$$

and

$$v^e = \frac{1}{\lambda} - v^a, \quad (30)$$

where the normalization variable

$$\lambda = \frac{1}{N} \text{Tr}(\mathbf{\Lambda}^H (\mathbf{\Lambda} \mathbf{\Lambda}^H v^a + \sigma^2 \mathbf{I}_N)^{-1} \mathbf{\Lambda}), \quad (31)$$

can be easily computed as shown in [14].

4) *Messages from DEM to DEC*: Lastly, the DEM node computes the extrinsic LLRs as input to the DEC node as

$$L_{n,b}^e = \ln \frac{\sum_{\mathbf{d} \in \mathcal{D}_b^{(0)}} D_n(\mathbf{d})}{\sum_{\mathbf{d} \in \mathcal{D}_b^{(1)}} D_n(\mathbf{d})} - L_{n,b}^a. \quad (32)$$

## B. Messages for the Sparse Precoders

The extension of the SILE-EPIC to the sparse precoders is fairly straightforward. The exchanged messages between the EQU and DEM nodes are now derived for the model of (7), which groups the symbols that are spread over the same set of sub-carriers. The messages exchanged between the DEM and DEC nodes remain unchanged since they do not directly depend on the modulation matrix.

1) *Messages from DEM to EQU*: The equation (26) is modified as

$$\bar{\gamma}_p^a = \frac{1}{Q} \sum_{n \in I_p} \gamma_n^a, \quad (33)$$

where the error variance is averaged only for indexes whose symbols share the same sub-carriers. Next, using the same subvectors<sup>3</sup> definition of Section III, we compute  $\mathbf{d}_p^*$  and  $v_p^*$  analogously to (27), where we now use  $\mu_p^a$ ,  $\mathbf{d}_p^e$ ,  $v_p^e$  and  $\bar{\gamma}_p^a$ . Then,  $\mathbf{d}_p^*$ ,  $v_p^*$ ,  $\mathbf{d}_p^e$  and  $v_p^e$  are applied analogously to the equation (28) to compute  $\mathbf{d}_p^a$  and  $v_p^a$ .

2) *Messages from EQU to DEM*: The message from the EQU to DEM  $(\mathbf{x}_p^e, v_p^e)$  are computed with equations (29), (30) and (31) by replacing  $\mathbf{d}^a$ ,  $v^a$ ,  $\mathbf{F}_N$ ,  $\mathbf{I}_N$ ,  $\mathbf{\Lambda}$  and  $N$  by  $\mathbf{x}_p^a$ ,  $v_p^a$ ,  $\mathbf{F}_Q$ ,  $\mathbf{I}_Q$ ,  $\mathbf{\Lambda}_p$  and  $Q$ , respectively. Obviously, for the SWH precoder,  $\mathbf{W}_Q$  is used instead of  $\mathbf{F}_Q$ .

## C. Scheduling

There are two iteration loops in the structure of the SILE-EPIC receiver, see Fig. 4. In particular, there is the self-iteration (SI) loop, which represents the messages exchanged by the EQU and DEM nodes, and there is the turbo iteration (TI) loop, which is related to the messages exchanged between the DEM and DEC nodes. Scheduling refers to the order in which these loops are performed. Defining the  $N_\tau$  and  $N_s$  as the maximum number of turbo and self-iteration, the indexes are conventionally defined as  $\tau \in \{0, 1, \dots, N_\tau\}$  and  $s \in \{0, 1, \dots, N_s\}$  to represent the turbo and self-iterations indexes, respectively. Thus, there are  $N_s + 1$  SIs for each TI index, which is determined empirically for a targeted performance and complexity trade-off.

## D. Comments on Full vs Sparse Spreading

In [6], the sparse spreading has been explored from the complexity perspective, where it has been shown that the equalizer's complexity is reduced from  $\mathcal{O}(N \log N)$  to  $\mathcal{O}(N \log Q)$ , which can be considerable since typically we can set  $Q \ll N$ . Another aspect that we investigate in this work is the performance gain due to a more accurate approximation of  $\gamma_p^a$  than  $\gamma^a$ . As shown in Appendix B, when the spreading precoding scheme is used,  $\gamma^a$  in (26) is averaged over the variance of all  $N$  data symbols, which is a worse approximation than the sparse spreading one,  $\gamma_p^a$  in (33), which averages over the subset of  $Q$  symbols.

<sup>3</sup>The  $p$ th subvector is related to the symbols that are spread over the same set of subcarriers.

TABLE I  
NUMBER OF REAL MULTIPLICATIONS AND ADDITIONS PER QAM SYMBOL.

Precoder and Receiver	Additions	Multiplications
SWH-Log-MAP	$(3 \log_2 J + 2)J^{\frac{Q}{2}} + 2(Q(\sqrt{J} - 1) + 1)$	$6(Q(\sqrt{J} - 1) + 1)$
SWH-Max-Log-MAP	$(\log_2 J + 2)J^{\frac{Q}{2}} + 2(Q(\sqrt{J} - 1) + 1)$	$4(Q(\sqrt{J} - 1) + 1)$
SWH-SILE-EPIC	$(N_s + 1)(4 \log_2 Q + \log_2 J + 7J + 6)$	$(N_s + 1)(8J + 11)$
DFT-SILE-EPIC	$(N_s + 1)(4 \log_2 Q + \log_2 J + 7J + 6)$	$(N_s + 1)(4 \log_2 Q + 8J + 11)$
SDFT-SILE-EPIC	$(N_s + 1)(4 \log_2 N + \log_2 J + 7J + 6)$	$(N_s + 1)(4 \log_2 N + 8J + 11)$

## VI. COMPLEXITY ANALYSIS

In the following, the complexity of the MAP and SILE-EPIC receivers respectively presented in Sections IV and V are derived in terms of real additions and multiplications per QAM symbol. The corresponding values are summarized in Table I. Also, the different methods are compared in terms of complexity in Section VII.

### A. Log-MAP for SWH

Starting with the number of additions, the computation of  $C_p^1(q', i)$  in (11) requires  $(Q(\sqrt{J} - 1) + 1)Q$  subtractions for all  $q' \in \{0, 1, \dots, Q - 1\}$  and  $i \in \{0, 1, \dots, (Q(\sqrt{J} - 1) + 1)\}$ , that is computed for a group of  $Q$  symbols. Also, there are  $QJ^{\frac{Q}{2}}$  additions to compute the sum over  $C_p^1(q', i)$  in (17) for all  $\mathbf{z} \in \mathcal{R}^Q$ . The incorporated sum of a-priori LLRs in (17) results in  $QJ^{\frac{Q}{2}} \frac{1}{2} \log_2 J$  additions for all  $\mathbf{z} \in \mathcal{R}^Q$ . Finally, since each symbol has  $\frac{1}{2} \log_2 J$  bits, there are  $2QJ^{\frac{Q}{2}} \frac{1}{2} \log_2 J$  additions for each group of  $Q$  symbols to compute the Log-SumExp using (19), as described in Subsection IV-C. Thus, the total amount of additions is found as  $2(\frac{3}{2} \log_2 J + 1)J^{\frac{Q}{2}} + 2(Q(\sqrt{J} - 1) + 1)$ , where the above terms have been added, multiplied by two to account for the in-phase and quadrature components, and divided by  $Q$  to have the quantity per symbol.

Regarding the multiplications, we see that  $C_{p,q'}(s_i)$  in (11) requires  $3(Q(\sqrt{J} - 1) + 1)Q$  multiplications for all  $q'$  and  $i$ , where the number 3 is multiplied to account for the element-wise products related to the channel, square exponent, and noise variance division. The final value of  $6(Q(\sqrt{J} - 1) + 1)$  is obtained by multiplying the above quantity by two to account for the in-phase and quadrature components, and dividing it by  $Q$  to have the quantity per symbol.

Although the overall complexity is considerably reduced due to the small number of multiplications, there are two important remarks to be made. Firstly, it is clear that this solution does not decrease the number of additions necessary to marginalize the posterior probability which scales with  $J^{\frac{Q}{2}}$ . Secondly, the receiver still needs to store the sets  $\mathcal{S}(\mathbf{z}, q)$  in a memory for each  $\mathbf{z}$ . Since there are  $J^{\frac{Q}{2}}$  possible realizations of  $\mathbf{z}$ , the number of values to be stored can be prohibitively high which also prevents the scalability of this detector. For the above reasons, the Log-MAP receiver for SWH is restricted to small values of  $Q$  and  $J$ , as shown in Section VII. Thus, it is clear that in order to expand the range of  $Q$  and  $J$  in which the Log-MAP can be implemented, it is necessary to mitigate these issues. In particular, the number of additions could be decreased by allowing only the values of  $\mathbf{z}$  which have a significant impact on the LogSumExp. Regarding the

memory sets  $\mathcal{S}(\mathbf{z}, q)$ , a possible approach to decrease the total amount of saved data could involve symmetries in the values of  $\mathbf{z}$ . A clear example is that for each  $\mathbf{z}$  there is a negative  $\mathbf{z}' = -\mathbf{z}$  which the index  $i' \in \mathcal{S}(\mathbf{z}', q)$  can be determined from  $\mathcal{S}(\mathbf{z}, q)$ . This simple approach decreases by half the amount of necessary values  $\mathcal{S}(\mathbf{z}, q)$  to be saved.

### B. Max-Log-MAP for SWH

For the Max-Log-Max method, a very similar approach to the previous subsection is taken, therefore we just highlight the differences with the Log-MAP. Regarding the number of additions, the Max-Log-MAP does not require the operations involved in the argument of  $f_c(|\delta_0 - \delta_1|)$ , thus it has  $2J^{\frac{Q}{2}} \log_2 J$  less additions per QAM symbol. For the number of multiplications, the values  $C_{p,q'}(s_i)$  in (11) can be computed with  $2(Q(\sqrt{J} - 1) + 1)$  multiplications where the number 2 is multiplied to account only for the element-wise products related to the channel and square exponent because the noise variance division can be done after the  $\max(\cdot)$  operation in (20).

For the same reasons discussed in the previous subsection, the Max-Log-MAP receiver is also restricted to small values of  $Q$  and  $J$ . Thus, future research should be made to allow a more diverse range of  $Q$  and  $J$ .

### C. SWH-SILE-EPIC

Firstly, we note that the a-priori symbol probability  $P_n(d)$  in equation (22) can be integrated into the computation of  $D_n(d)$  in (23). Thus, (23) needs  $\log_2 J$  due to (22),  $2J$  due to the argument of (23)<sup>4</sup> for all  $d \in \mathcal{S}$  and  $J$  to normalize (23). Equations (24), (25), (26), (27) and (28) requires,  $2J$ ,  $2J + 1$ , 1, 2 and 2, respectively. Adding the above components and multiplying the number of self iterations  $N_s$ , we find that  $N_s(\log_2 J + 7J + 6)$  additions per symbol to compute the message from the DEM to EQU ( $\mathbf{x}^e, v^e$ ). In order to compute the operations spent in (29), only the complexity of the modulation  $\mathbf{W}_Q$  is considered for simplicity. We note that  $\mathbf{W}_Q$  requires  $2N \log_2 Q$  real addition [6]. Since it is called two times, by dividing it by  $N$ , we find  $2 \log_2 Q$  additions for the precoding. Since the above operations are computed for each iteration index  $s \in \{0, 1, \dots, N_s\}$ , they are processed  $(N_s + 1)$  number of times in total. Thus, from the equation (23) to (29), there are  $(N_s + 1)(4 \log_2 Q + \log_2 J + 7J + 6)$  real additions.

Regarding the amount of multiplications, equation (23) require  $2J^5$  operations due to the square  $(\cdot)^2$ , and  $J v^e$  for all

<sup>4</sup>Additions (or subtractions) between two complex numbers count twice.

<sup>5</sup>The square of a complex counts two multiplications.

$d \in \mathcal{S}$  and  $J$  to normalize (23). The remaining equations (24), (25), (27) and (28) require  $2J^6$ ,  $2J+1$ , 6 and 4, respectively. Adding the above components and multiplying the number of self-iterations  $N_s$ , we find that  $N_s(6J+11)$  additions per symbol to compute the message from the DEM to EQU. Regarding the equalizer in (29),  $\mathbf{W}_Q$  spends no multiplication, thus the overall multiplication amount is  $(N_s+1)(8J+11)$ .

#### D. SDFT-SILE-EPIC

The amount of additions spent by the SDFT-SILE-EPIC is exactly the same as SWH-SILE-EPIC. Basically, the number of additions and multiplications spent from equation (23) to (28) is the same regardless of the precoder. And the equalizer in (29), the amount of additions is also the same as SWH because the transformation is done with the same size. Thus, the SDFT-SILE-EPIC consumes  $(N_s+1)(4\log_2 Q + \log_2 J + 7J + 6)$  real additions.

For the multiplications, the DFT consumes  $2N\log_2 Q$  real multiplications<sup>7</sup>. Since it is called twice in (29), there are  $4\log_2 Q$  more multiplications in the SDFT than in the SWH per QAM symbol, which is  $(N_s+1)(4\log_2 Q + 6J + 11)$ .

#### E. DFT-SILE-EPIC

Again, what changed from SDFT to DFT, is the transformation  $\mathbf{F}_N$  in (29) instead of  $\mathbf{F}_Q$ . Thus, comparing with the results valued for SDFT-SILE-EPIC, it is straightforward to derive the number of additions and multiplications for the DFT-SILE-EPIC respectively as  $(N_s+1)(4\log_2 N + \log_2 J + 7J + 6)$  and  $(N_s+1)(4\log_2 N + 6J + 11)$ .

### VII. NUMERICAL EVALUATION

Simulation parameters are described in Table II. The amount of QAM symbols per transmission is  $N = 256$ . The channel is the highly frequency selective Proakis-C impulse response  $h = [0.23 \ 0.46 \ 0.69 \ 0.46 \ 0.23]^T$  with maximum delay of  $L = 5$  samples. In the frequency domain, the channel is  $\text{diag}(\mathbf{\Lambda}) = \text{DFT}_N(h)$  with zero on its off-diagonals. We set  $Q = \{4, 8\}$  for the sparse spreading precoding schemes. Notice that the condition  $Q \geq L$  [6] is respected only for  $Q = 8$ . Regarding the encoder and decoder, the  $R = 1/2$  code rate recursive systematic convolutional (RSC) code is employed with polynomial  $[1, 5/7]_8$ , and the SISO decoder is used with BCJR algorithm. The number of turbo iterations is set  $N_\tau = 9$  for all cases.

The systems are evaluated in terms of frame error rate (FER) and extrinsic information transfer (EXIT) chart. The EXIT chart analyses the asymptotic behavior of the system [33], which is meaningful under the assumptions of long codeword and a high number of turbo iterations. In addition, the EXIT chart provides an assessment of the equalizer independently of the encoder and decoder, making the conclusions more general. The detector's asymptotic behavior is characterized

<sup>6</sup>Multiplications (or divisions) between real and complex numbers count twice.

<sup>7</sup>The  $Q$ -size FFT consumes  $1/2Q\log_2 Q$  complex multiplications, which is multiplied by 4 to account for real multiplications.

TABLE II  
SIMULATION PARAMETERS.

Parameter	Value
number of symbols per block	$N = 256$
channel	Proakis-C, $L = 5$
spreading parameter	$Q = \{4, 8\}$
QAM order	$J = \{4, 16, 64\}$
code rate	$R = 1/2$
encoder	RSC $[1, 5/7]_8$
decoder	SISO BCJR (log-MAP)

TABLE III  
NUMBER OF REAL ADDITIONS PER QAM SYMBOL.

Precoder and Receiver		QPSK	16-QAM	64-QAM
SWH	$Q = 4$	138	3,610	81,978
Log-MAP	$Q = 8$	2,066	917,554	335,544,434
SWH	$Q = 4$	74	1,562	32,826
Max-Log-MAP	$Q = 8$	1,042	393,266	134,217,842
SWH-SILE-EPIC	$Q = 8$	144	804	3,304
SDFT-SILE-EPIC	$Q = 8$	144	804	3,304
DFT-SILE-EPIC		204	924	3,444

TABLE IV  
NUMBER OF REAL MULTIPLICATIONS PER QAM SYMBOL.

Precoder and Receiver		QPSK	16-QAM	64-QAM
SWH	$Q = 4$	30	78	174
Log-MAP	$Q = 8$	54	150	342
SWH	$Q = 4$	20	52	116
Max-Log-MAP	$Q = 8$	36	100	228
SWH-SILE-EPIC	$Q = 8$	129	834	3,661
SDFT-SILE-EPIC	$Q = 8$	165	906	3,745
DFT-SILE-EPIC		225	1,026	3,885

by the transfer curve  $I_{E,\text{det}} = \mathcal{T}_{\text{det}}(I_{A,\text{det}})$ , where  $I_{E,\text{det}}$  and  $I_{A,\text{det}}$  are the mutual information (MI) between the coded data with the a-priori and extrinsic LLRs, respectively. A typical approach to compute  $\mathcal{T}_{\text{det}}(I_{A,\text{det}})$  and  $I_{E,\text{dec}} = \mathcal{T}_{\text{dec}}(I_{A,\text{dec}})$  is to assume Gaussian distributed LLRs in the input of the respective blocks, i.e., detector and decoder. However, in practice the LLRs' distributions differ from the Gaussian assumption, so the convergence of iterative receivers can be analyzed with the MI trajectories w.r.t. the turbo iterations using finite length simulations [34], where the inverse transfer curve of the decoder  $\mathcal{T}_{\text{dec}}^{-1}(I_{A,\text{det}})$  is also plotted, which are computed in relatively high SNR such that we are able to observe the receiver's convergence.

#### A. Evaluation of MAP receivers for SWH

The MAP detectors for the SWH precoder shown in Section IV are compared in terms of FER in Fig. 5. Firstly, we note that there is no performance loss in using the Log-MAP approximation in IV-C compared to the general receiver of [27]. This result is expected since the Log-MAP approximation using the look-up table to compute  $f_c(|\delta_0 - \delta_1|)$  is known to be accurate as shown in [28]. Regarding the Max-Log-MAP approximation, its implementation incurs a slight performance loss in relation to the Log-MAP of approximately 0.3 dB for

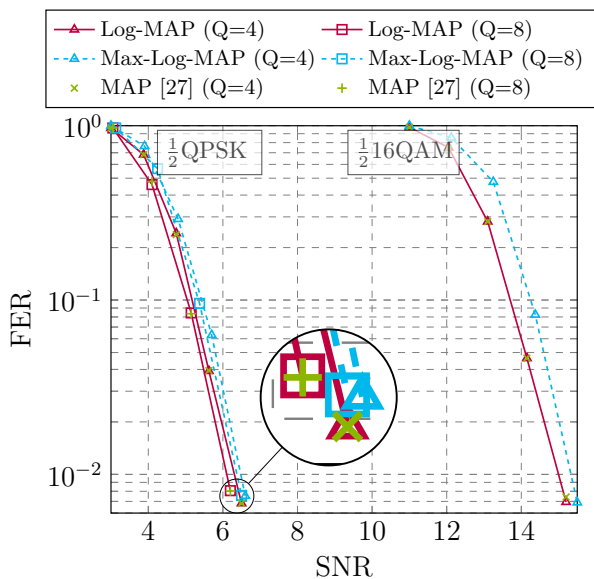


Fig. 5. Comparison between Log-MAP and Max-Log-MAP methods of the SWH detector described in Section IV.

QPSK with  $Q = 8$  and 16-QAM  $Q = 4$  for  $\text{FER} = 10^{-2}$ . The gap is decreased for QPSK with  $Q = 4$ . These results indicate that the gap between the Log-MAP and Max-Log-MAP increases for higher  $Q$  or  $J$ , which happens because the number of ignored  $t_p^1(\mathbf{z})$  values in (18) increases. In addition, examining the EXIT chart depicted in Fig. 6, the Max-Log-MAP performance loss occurs due to the first iteration in all cases. In order to make this analysis more clear for the QPSK modulation, we magnified the results for  $I_{E,\text{det}} = \mathcal{T}_{\text{det}}^{-1}(I_{A,\text{det}})$  for  $I_{A,\text{det}} = 0$ , where one can observe that  $I_{E,\text{det}}$  is higher for the Log-MAP method (red straight line). For the 16-QAM results, the difference is more prominent. Basically, the Log-MAP equalizer feeds the decoder with LLRs that have higher MI with the coded data, leading to faster convergence in correctly detecting the transmitted codeword, which can be verified by the MI trajectories.

The number of real additions and multiplications are shown in Tables III and IV, respectively. Comparing the Max-Log-MAP against Log-MAP, we observe that the number of additions is decreased by approximately half in all cases, and the number of multiplications is decreased exactly by 1/3, which is clear from Table I. Since the performance is not decreased considerably, it makes the Max-Log-MAP method appealing in practical systems. For the sake of completeness, we have also included the complexity for  $J = 64$ . While the number of multiplications remains low, the number of additions increases exponentially with  $J^{\frac{Q}{2}}$  and becomes impractical. As discussed in [27], this highlights the limitations of the MAP receiver when  $Q$  or  $J$  increases. For the current approaches presented in this work, both Log-MAP and Max-Log-MAP methods are feasible for QPSK with  $Q = 4$  and 8, and 16-QAM with  $Q = 8$ . The bottleneck that limits the receiver is discussed in detail in Subsection VI-A, where directions to tackle this issue are provided for future works.

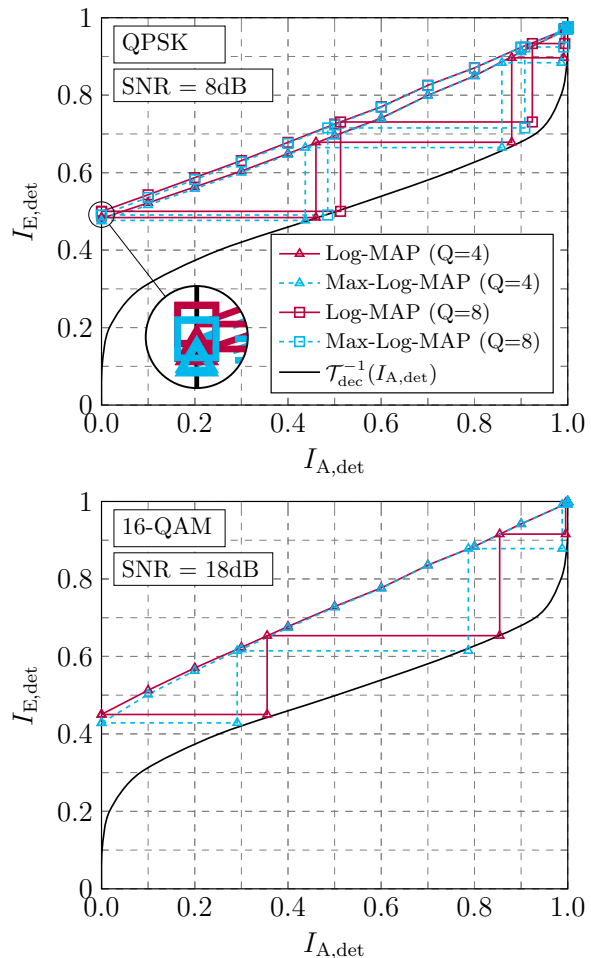


Fig. 6. Comparison between Log-MAP and Max-Log-MAP methods of the SWH detector described in Section IV.

## B. Evaluation of Systems Employing SILE-EPIC

This subsection investigates two different aspects, namely, i) the impact of sparsity using the DFT precoding, and ii) the comparison between the DFT vs WHT precoders with sparsity for  $Q = 8$ . We set  $\beta$  in (28) as follows. Defining  $N_\tau$  and  $N_s$  as the maximum number of turbo and self-iteration, the indexes  $\tau \in \{0, 1, \dots, N_\tau\}$  and  $s \in \{0, 1, \dots, N_s\}$  represent the turbo and self-iterations indexes, respectively. In this work, our goal is not to optimize the best  $\beta$  values, therefore we use the same formula as [21] which depends on the iteration indexes  $(\tau, s)$ . In particular, we use  $\beta_{\tau,s} = 0.7 \cdot 0.9^{\tau+s}$  for QPSK,  $\beta_{\tau,s} = 0.85 \cdot 0.85^{\tau+s}$  for 16-QAM and  $\beta_{\tau,s} = 0.85^{\tau+s}$  for 64-QAM. Lastly, the QPSK, 16-QAM, and 64-QAM modulations have respectively  $N_s = 2, 5$  and 6 self-iterations (SIs).

Firstly, it is observed in Fig. 7 that the SDFT system slightly outperforms the conventional DFT system. As explained in Subsection V-D, the system with sparsity has a better approximation to the a-priori variance of the data symbols. This leads to a slight, but noticeable, improvement of approximately 0.3 dB at  $\text{FER} = 10^{-2}$  for the systems with QPSK and 64-QAM, and 0.1 dB for the 16-QAM. The results are also verified in the EXIT chart for 16-QAM, where we see that  $\mathcal{T}_{\text{det}}(0)$  is slightly higher for the SDFT system, which is sufficient to provoke faster receiver convergence, resulting in

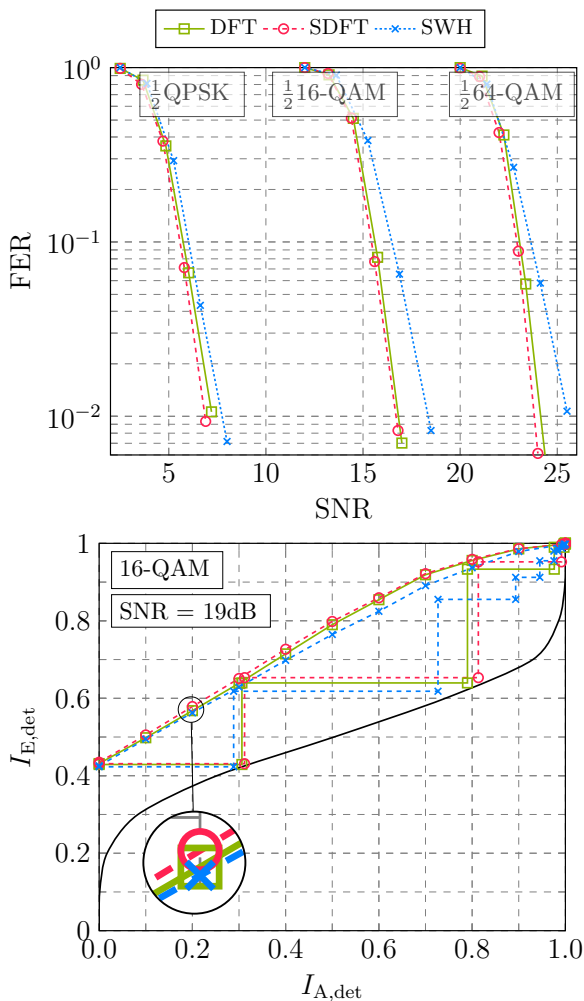


Fig. 7. FER and EXIT curves for (S)DFT and SWH precoders with the SILE-EPIC receiver of [21] described in V. QPSK, 16-QAM and 64-QAM have respectively  $N_s = 2, 5$  and 6 self-iterations (SIs).

not only a better performance, but also decreasing the number of necessary turbo iterations. Although it is not shown here, we have observed that this behavior is maintained for many other configurations of  $\beta_{\tau,s}$ , indicating that this is a general behavior.

Secondly, it is observed in Fig. 7 that the SWH system performs worse than the SDFT scheme when both use the SILE-EPIC receiver. In particular, for the FER of  $10^{-2}$ , 1dB loss is observed for QPSK and 2dB loss occurs for 16-QAM and 64-QAM. Additionally, the EXIT chart also depicts the lack of convergence of the SWH system in comparison to the DFT systems, which is complementary to the FER curves. This result has not been observed in previous works [6], where both SWH and DFT waveforms performed equally. Thus, the outcomes presented in this paper suggest that for highly selective channels such as the Proakis-C, the equal gain condition [10] is not the only factor that determines the performance of a given waveform. A detailed investigation on this topic is out of the scope of our work, however, a logical explanation is that the different ISI patterns of both precoders at the receiver can be the cause for the performance

discrepancy.

In terms of the complexity analysis shown in Tables III and IV, it is observed that for QPSK, there are approximately 25% of additions and multiplications savings by using SDFT instead of the DFT. However, as the QAM order increases to 16-QAM and 64-QAM, the savings become negligible, because the constellation order  $J$  plays a major role than the spreading parameter  $Q$ , as one can see in Table I. The same effect happens when comparing SWH to SDFT. Basically, SWH can save approximately 25% of multiplications for QPSK, but these savings also become negligible for higher  $J$ .

In conclusion, considering the performance gain and computational savings, the results of this analysis favor the SDFT precoder over DFT, especially for QPSK where the reduction in complexity is about 25%. Lastly, the SDFT precoder also outperforms the SWH with the SILE-EPIC, however, a more general comparison is made in the subsequent subsection where the SWH is compared using the MAP receivers of Section IV.

### C. Performance and Complexity trade-off Between (S)DFT and SWH Precoders

Although the SWH system performs worse than DFT system when both employ the SILE-EPIC, SWH has the advantage of being able to employ the MAP detector with reasonable implementation complexity. Thus, it is worth comparing both systems with their best available receiver options, where the SWH with the Max-Log-MAP method is shown. These results are shown in Fig. 8.

For completeness, we include the results of the VAMP implementation [30] in this analysis. In particular, we implemented the LMMSE version described by Algorithm 3 in [30], whose main difference from the SILE-EPIC is situated in the damping procedure of equation (28), as noted in [21]. Specifically, the damping of VAMP is described in [30, (26-27)], which for the SILE-EPIC translates into combining  $\mu_n^a$  and  $v^e$  in (24) and (30), respectively, with their respective values of previous self-iterations. Lastly, since VAMP uses the same blocks as SILE-EPIC, its complexity is of the same order. In summary, the results depicted in Fig. 8 confirm the outcomes of [21], where the SILE-EPIC shows superior performance than VAMP. In addition, we note that the performance gap is smaller for the SDFT than the DFT precoder, and the gap diminishes with higher QAM.

For the QPSK and 16-QAM modulations, the SWH with MAP receivers have approximately 1dB and 2dB gains, respectively, over the DFT system for the FER of  $10^{-2}$ . This gap is slightly decreased when compared to the SDFT. Regarding the complexity collected from Tables III and IV, we observe that for QPSK and  $Q = 4$ , the Max-Log-MAP spends 74 additions and 20 multiplications, while the SDFT-SILE-EPIC system spends 144 additions and 165 multiplications. Comparing both, we see that the Max-Log-MAP receiver spends 50% on additions and 12% on multiplications, which shows an overall complexity reduction. However, for the configuration with  $Q = 8$ , the Max-Log-MAP number of additions are multiplications are 1,042 and 36, respectively. While the number

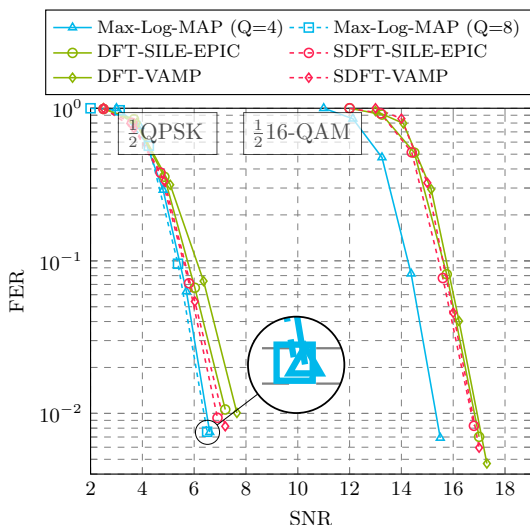


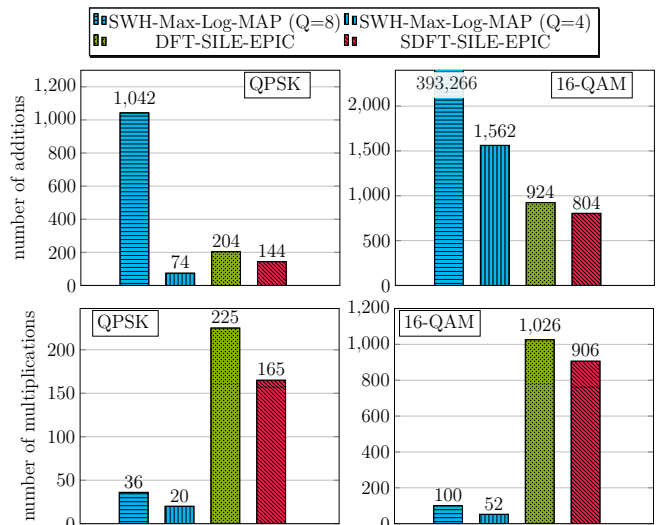
Fig. 8. Performance and complexity trade-off between SWH-Max-Log-MAP and (S)DFT-SILE-EPIC. The FER results for the VAMP based equalizer [30] are shown for completeness.

of multiplications remains low, the number of additions now is 7.24 times higher than the SDFT-SILE-EPIC, such that the complexity reduction is no more present. Analyzing now the 16-QAM system with  $Q = 4$ , the Max-Log-MAP method spends 1,562 additions and 52 multiplications, respectively, while the SDFT-SILE-EPIC spends 804 and 906. In absolute terms, the Max-Log-MAP spends 758 more additions and 662 fewer multiplications. Given that multiplications are more costly computationally, we can conclude that in this case, the Max-Log-MAP provides lower complexity than the SDFT-SILE-EPIC for 16-QAM and  $Q = 4$ .

In conclusion, the performance and complexity trade-off analysis favors the SWH precoder with Max-Log-MAP receiver when  $Q = 4$  is utilized for both QPSK and 16-QAM. For  $Q = 8$  with QPSK, the number of additions required by the Max-Log-MAP receiver surpasses the SILE-EPIC considerably, while the performance gain is marginal, meaning that setting  $Q = 4$  provides a good trade-off. For all other configurations, namely, 16-QAM with  $Q = 8$  and 64-QAM, the Max-Log-MAP receiver complexity is very high in terms of additions, which limits its employment in those cases, which favors other implementations and/or precoders such as the SDFT-SILE-EPIC.

### VIII. CONCLUSION

In this work, we have provided two feasible methods for the SWH MAP detector, namely, Log-MAP and Max-Log-MAP. While the Max-Log-MAP has a slight performance loss in relation to the Log-MAP, the number of additions and multiplications are decreased respectively by 1/2 and 1/3, which makes the Max-Log-MAP appealing in practice. Another aspect of this paper consisted in investigating the impact of SDFT, DFT, and SWH precoder employing the SILE-EPIC receiver. The results have revealed that the SDFT system provides slightly better performance than the conventional DFT system with 25% less complexity than the conventional DFT system for QPSK. Lastly, the performance and complexity trade-offs



between SWH-Max-Log-MAP and (S)DFT-SILE-EPIC have been investigated. The results show that for QPSK and 16-QAM constellations, SWH-Max-Log has a better trade-off when setting the spreading parameter to  $Q = 4$ .

For future work, we propose to investigate alternatives to decrease the complexity of the Max-Log-MAP detector for SWH even more, since its implementation is not feasible for  $Q \geq 8$  with 16 order QAM or above, which limits its range of application. Another interesting open point is the extension of the Max-Log-MAP for MIMO systems. In particular, the detector provided in this work can be used to detect signal per transmit antenna with interference cancellation. Since the evaluation of this work is constrained to a highly frequency selective channel model, it is of interest to conduct this investigation under other types of channels, including time selectivity.

### APPENDIX A

#### MULTIPLICATIONS REDUCTION OF MAP DETECTOR

In the following, we show that the norm present in (10) can be computed as

$$-\frac{1}{\sigma^2} \|\mathbf{y}_p^I - |\Lambda_p| \mathbf{W}_Q \mathbf{z}\|^2 = \sum_{\substack{q=0, \\ i=S(\mathbf{z}, q)}}^{Q-1} C_p^I(q, i). \quad (34)$$

Let  $\tilde{\mathbf{u}} = \tilde{\mathbf{W}}_Q \mathbf{z}$ , where  $\tilde{\mathbf{W}}_Q$  is the non normalized Walsh-Hadamard matrix of size  $Q \times Q$ ,  $\mathbf{z} \in \mathcal{R}^Q$  is the PAM vector of size  $Q$  and

$$\mathcal{R} = \left\{ -\sqrt{J} + 1 + 2i | i \in \{0, 1, \dots, \sqrt{J} - 1\} \right\} \quad (35)$$

is the PAM constellation set with cardinality  $|\mathcal{R}| = \sqrt{J}$ . It has been shown in [27], that all possible elements of  $\tilde{\mathbf{u}}$  belong to the set

$$\mathcal{U} = \left\{ -Q(\sqrt{J}-1) + 2i | i \in \{0, 1, \dots, Q(\sqrt{J}-1)\} \right\} \quad (36)$$

that has cardinality  $|\mathcal{U}| = Q(\sqrt{J} - 1) + 1$ . The vector  $\mathbf{s}$  with elements taken from  $\mathcal{U}$  without repetition can be defined as

$$s_i = (-Q(\sqrt{J} - 1) + 2i) / \sqrt{Q} \quad (37)$$

for  $i \in \{0, 1, \dots, Q(M-1)\}$ . The division  $\sqrt{Q}$  assumes a normalized WH transformation.

Now, for a realization  $\mathbf{z}$  and  $\mathbf{u} = \mathbf{W}_Q \mathbf{z}$ , we can define the quantity  $C_p^I(q, i)$  based on  $s_i$  in (37) as

$$\begin{aligned} C_p^I(q, i) &= -\frac{1}{\sigma^2} (\mathbf{y}_p^I[q] - |\mathbf{\Lambda}_p[q, q]| u_q)^2 \\ &= -\frac{1}{\sigma^2} (\mathbf{y}_p^I[q] - \mathbf{\Lambda}_p[q, q] s_i)^2, \end{aligned} \quad (38)$$

for  $p \in \{0, 1, \dots, P-1\}$  and  $q \in \{0, 1, \dots, Q-1\}$ .

From (38), it is clear that (34) holds. In (10) and (34), the set  $\mathcal{S}(\mathbf{z}, q) = \{i | u_q = s_i\}$  returns the index  $i$  which attains the condition  $u_q = s_i$  and can be interpreted as a database which stores the respective values for all  $\mathbf{z} \in \mathcal{R}^Q$  and  $q \in \{0, 1, \dots, Q-1\}$ .

## APPENDIX B

### ACCURACY OF SYMBOL VARIANCE APPROXIMATION

The accuracy of  $\bar{\gamma}^a$  in (26) and  $\bar{\gamma}_p^a$  in (33) can be described in terms of their mean squared errors (MSEs). For the MSE of  $\bar{\gamma}^a$  we can write

$$\begin{aligned} \text{MSE} &= \frac{1}{N} \sum_{n=0}^{N-1} (\gamma_n^a)^2 - \left( \frac{1}{N} \sum_{n=0}^{N-1} \gamma_n^a \right)^2 \\ &= \frac{1}{N} \sum_{n=0}^{N-1} (\gamma_n^a)^2 - \left( \frac{1}{P} \sum_{p=0}^{P-1} \bar{\gamma}_p^a \right)^2, \end{aligned} \quad (39)$$

where the second line is obtained by replacing  $\frac{1}{N} \sum_{n=0}^{N-1} \gamma_n^a$  by  $\frac{1}{P} \sum_{p=0}^{P-1} \bar{\gamma}_p^a$ . The average MSE for the system with sparsity  $\bar{\gamma}_p^a$  is written as

$$\begin{aligned} \text{MSE}_s &= \frac{1}{P} \sum_{p=0}^{P-1} \left( \frac{1}{Q} \sum_{n \in I_p} (\gamma_n^a)^2 - \left( \frac{1}{Q} \sum_{n \in I_p} \gamma_n^a \right)^2 \right), \\ &= \frac{1}{N} \sum_{n=0}^{N-1} (\gamma_n^a)^2 - \frac{1}{P} \sum_{p=0}^{P-1} (\bar{\gamma}_p^a)^2. \end{aligned} \quad (40)$$

Our goal is to show that  $\text{MSE}_s \leq \text{MSE}$ . From the above equations, this inequality implies  $\left( \frac{1}{P} \sum_{p=0}^{P-1} \bar{\gamma}_p^a \right)^2 \leq \frac{1}{P} \sum_{p=0}^{P-1} (\bar{\gamma}_p^a)^2$ , which holds due to Jensen's inequality since  $f(x) = x^2$  is a convex function for  $x \in \mathbb{R}_{\geq 0}$ .

## REFERENCES

- [1] R. Hadani, S. Rakib, M. Tsatsanis, A. Monk, A. J. Goldsmith, A. F. Molisch, and R. Calderbank, "Orthogonal Time Frequency Space Modulation," in *2017 IEEE Wireless Communications and Networking Conference (WCNC)*, pp. 1–6, March 2017.
- [2] R. Bomfin, M. Chafii, A. Nimr, and G. Fettweis, "A robust baseband transceiver design for doubly-dispersive channels," *IEEE Trans. Wireless Commun.*, vol. 20, no. 8, pp. 4781–4796, 2021.
- [3] X. Ouyang and J. Zhao, "Orthogonal Chirp Division Multiplexing," *IEEE Trans. Commun.*, vol. 64, pp. 3946–3957, Sept 2016.
- [4] T. Zemen, M. Hofer, D. Löschenbrand, and C. Pacher, "Iterative Detection for Orthogonal Precoding in Doubly Selective Channels," in *2018 IEEE 29th Annual International Symposium on Personal, Indoor and Mobile Radio Communications (PIMRC)*, pp. 1–7, 2018.
- [5] T. Thaj, E. Viterbo, and Y. Hong, "Orthogonal time sequency multiplexing modulation: Analysis and low-complexity receiver design," *IEEE Transactions on Wireless Communications*, vol. 20, no. 12, pp. 7842–7855, 2021.
- [6] R. Bomfin, A. Nimr, M. Chafii, and G. Fettweis, "A Robust and Low-Complexity Walsh-Hadamard Modulation for Doubly-Dispersive Channels," *IEEE Commun. Lett.*, vol. 25, no. 3, pp. 897–901, 2021.
- [7] M. Chafii, L. Bariah, S. Muhaidat, and M. Debbah, "Twelve scientific challenges for 6g: Rethinking the foundations of communications theory," *IEEE Communications Surveys & Tutorials*, pp. 1–1, 2023.
- [8] H. G. Myung, J. Lim, and D. J. Goodman, "Peak-To-Average Power Ratio of Single Carrier FDMA Signals with Pulse Shaping," in *2006 IEEE 17th International Symposium on Personal, Indoor and Mobile Radio Communications*, pp. 1–5, 2006.
- [9] Y. Carmon, S. Shamai, and T. Weissman, "Comparison of the achievable rates in ofdm and single carrier modulation with i.i.d. inputs," *IEEE Transactions on Information Theory*, vol. 61, pp. 1795–1818, April 2015.
- [10] R. Bomfin, D. Zhang, M. Matthé, and G. Fettweis, "A Theoretical Framework for Optimizing Multicarrier Systems Under Time and/or Frequency-Selective Channels," *IEEE Commun. Lett.*, vol. 22, pp. 2394–2397, Nov 2018.
- [11] F. Burmeister, N. Schwarzenberg, T. Höbner, and G. Fettweis, "Measuring time-varying industrial radio channels for d2d communications on agvs," in *2021 IEEE Wireless Communications and Networking Conference (WCNC)*, pp. 1–7, 2021.
- [12] S. Wang, S. Zhu, and G. Zhang, "A walsh-hadamard coded spectral efficient full frequency diversity ofdm system," *IEEE Transactions on Communications*, vol. 58, no. 1, pp. 28–34, 2010.
- [13] M. Tuchler, R. Koetter, and A. C. Singer, "Turbo equalization: principles and new results," *IEEE Trans. Commun.*, vol. 50, no. 5, pp. 754–767, 2002.
- [14] R. Bomfin, M. Chafii, and G. Fettweis, "Low-Complexity Iterative Receiver for Orthogonal Chirp Division Multiplexing," in *IEEE WCNC workshops*, (Marrakech, Morocco), Apr. 2019.
- [15] F. Long, K. Niu, C. Dong, and J. Lin, "Low Complexity Iterative LMMSE-PIC Equalizer for OTFS," in *ICC 2019 - 2019 IEEE International Conference on Communications (ICC)*, pp. 1–6, 2019.
- [16] C. Douillard, M. Jezequel, and C. Berrou, "Iterative correction of intersymbol interference: Turbo equalization," *Eur. Trans. Telecommun.*, vol. 6, no. 5, pp. 507–511, 1995.
- [17] D. Raphaeli and A. Saguy, "Linear equalizers for turbo equalization: A new optimization criterion for determining the equalizer taps," in *Proc. Int. Symp. Turbo Codes Related Topics*, pp. 371–374, 2000.
- [18] M. Matthé, D. Zhang, and G. Fettweis, "Low-Complexity Iterative MMSE-PIC Detection for MIMO-GFDM," *IEEE Trans. Commun.*, vol. 66, pp. 1467–1480, April 2018.
- [19] C. Studer, S. Fateh, and D. Seethaler, "ASIC Implementation of Soft-Input Soft-Output MIMO Detection Using MMSE Parallel Interference Cancellation," *IEEE J. Solid-State Circuits*, vol. 46, pp. 1754–1765, July 2011.
- [20] L. Fang, L. Xu, and D. D. Huang, "Low Complexity Iterative MMSE-PIC Detection for Medium-Size Massive MIMO," vol. 5, no. 1, pp. 108–111, 2016.
- [21] S. Şahin, A. M. Cipriano, C. Poulliat, and M.-L. Boucheret, "A framework for iterative frequency domain ep-based receiver design," *IEEE Trans. Commun.*, vol. 66, no. 12, pp. 6478–6493, 2018.
- [22] S. Şahin, A. M. Cipriano, C. Poulliat, and M. Boucheret, "Iterative equalization with decision feedback based on expectation propagation," *IEEE Transactions on Communications*, vol. 66, no. 10, pp. 4473–4487, 2018.
- [23] I. Santos, J. J. Murillo-Fuentes, R. Boloix-Tortosa, E. Arias-de Reyna, and P. M. Olmos, "Expectation propagation as turbo equalizer in isi channels," *IEEE Trans. Commun.*, vol. 65, no. 1, pp. 360–370, 2017.
- [24] I. Santos, J. J. Murillo-Fuentes, E. Arias-de Reyna, and P. M. Olmos, "Turbo ep-based equalization: A filter-type implementation," *IEEE Trans. Commun.*, vol. 66, no. 9, pp. 4259–4270, 2018.
- [25] D. Zhang and L. L. Mendes and M. Matthé and I. S. Gaspar and N. Michailow and G. P. Fettweis, "Expectation Propagation for Near-Optimum Detection of MIMO-GFDM Signals," *IEEE Trans. Wireless Commun.*, vol. 15, pp. 1045–1062, Feb 2016.
- [26] K. Wu, G. Ren, X. Meng, J. Wu, and Q. Wang, "Spectral-efficient band allocation scheme for frequency-domain pulse-shaping-based sc-fdma

- systems,” *IEEE Trans. Veh. Technol.*, vol. 66, no. 9, pp. 8249–8262, 2017.
- [27] R. Bomfin, M. Chaffi, A. Nimr, and G. P. Fettweis, “Maximum a-posteriori equalizer for sparse walsh hadamard modulation,” in *2022 IEEE Global Communications Conference: Signal Processing for Communications (GlobeCom 2022 SPC)*, (Rio de Janeiro, Brazil), Dec. 2022.
- [28] P. Robertson, E. Villebrun, and P. Hoeher, “A comparison of optimal and sub-optimal map decoding algorithms operating in the log domain,” in *Proceedings IEEE International Conference on Communications ICC '95*, vol. 2, pp. 1009–1013 vol.2, 1995.
- [29] Q. Guo, D. Huang, S. Nordholm, J. Xi, and Y. Yu, “Iterative frequency domain equalization with generalized approximate message passing,” *IEEE Signal Processing Lett.*, vol. 20, no. 6, pp. 559–562, 2013.
- [30] S. Rangan, P. Schniter, and A. K. Fletcher, “Vector approximate message passing,” *IEEE Trans. Inf. Theory*, vol. 65, no. 10, pp. 6664–6684, 2019.
- [31] G. Caire, G. Taricco, and E. Biglieri, “Bit-interleaved coded modulation,” *IEEE Trans. Inf. Theory*, vol. 44, no. 3, pp. 927–946, 1998.
- [32] M. Huemer and O. Lang, “On component-wise conditionally unbiased linear bayesian estimation,” in *2014 48th Asilomar Conference on Signals, Systems and Computers*, pp. 879–885, 2014.
- [33] S. Ten Brink, “Designing iterative decoding schemes with the extrinsic information transfer chart,” *AEU-International Journal of Electronics and Communications*, vol. 54, no. 5, pp. 279–286, 2000.
- [34] J. Hagenauer, “The exit chart - introduction to extrinsic information transfer in iterative processing,” in *2004 12th European Signal Processing Conference*, pp. 1541–1548, 2004.